

Trojan bacteria cross blood-brain barrier for glioblastoma photothermal immunotherapy

Rong Sun

Soochow University

Mingzhu Liu

Soochow University

Jianping Lu

Soochow University

Binbin Chu

Soochow university

Yunmin Yang

Soochow University

Bin Song

Soochow University

Houyu Wang

Soochow university

Yao He (✉ yaohe@suda.edu.cn)

Soochow University

Article

Keywords:

Posted Date: December 10th, 2021

DOI: <https://doi.org/10.21203/rs.3.rs-1114519/v1>

License:  This work is licensed under a Creative Commons Attribution 4.0 International License.

[Read Full License](#)

Version of Record: A version of this preprint was published at Nature Communications on September 1st, 2022. See the published version at <https://doi.org/10.1038/s41467-022-32837-5>.

Abstract

Bacteria can bypass the blood-brain barrier (BBB) transcellularly, paracellularly and/or in infected phagocytes, suggesting the possibility of employment of bacteria for combating central nervous system (CNS) diseases. However, the bacteria-based drug delivery vehicle crossing the BBB is still vacant up to present. Herein, we develop an innovative bacteria-based drug delivery system (dubbed Trojan bacteria) for glioblastoma (GBM) photothermal immunotherapy. Typically, Trojan bacteria are made of therapeutics internalized into bacteria (e.g., attenuated *Salmonella typhimurium*, *Escherichia coli*). The therapeutics are composed of glucose polymer (GP) (e.g., poly[4-O-(α -D-glucopyranosyl)-D-glucopyranose])-conjugated and indocyanine green (ICG)-loaded silicon nanoparticles (GP-ICG-SiNPs). The GP-ICG-SiNPs can be selectively and robustly internalized into the bacterial intracellular volume through the bacteria-specific ATP-binding cassette (ABC) transporter. In an orthotopic GBM mouse model, we demonstrate that the intravenously injected Trojan bacteria could take therapeutics together not only to bypass the BBB, but also to target and penetrate GBM tissues. Under 808 nm-laser irradiation, the photothermal effects (PTT) produced by ICG allow the destruction of Trojan bacterial cells and the adjacent tumour cells. Furthermore, the bacterial debris as well as the tumour-associated antigens would promote antitumor immune responses that prolong the survival of GBM-bearing mice. Moreover, we demonstrate the residual Trojan bacteria could be effectively eliminated from the body due to the distinct photothermal effects. We anticipate the proposed Trojan bacteria system would catalyze innovative therapies for various CNS diseases.

Introduction

Central nervous system (CNS) tumours are still a significant cause of morbidity and mortality throughout the world. For example, glioblastoma (GBM) is the most aggressive brain tumour, with more than 15,000 deaths each year in the United States alone, and a 5-year survival rate of less than 10%¹⁻⁴. One key challenge in the therapy of GBM is to develop a high-efficiency drug delivery system (DDS) bypassing the blood-brain barrier (BBB), which is impermeable to most drugs⁵⁻⁷. For example, the levels of antibodies in the brain are only 0.01–0.1% of those in plasma after parenteral administration^{8,9}. To delivery drugs into brain, invasive and non-invasive technologies have been proposed¹⁰⁻¹⁴. The invasive approaches include deep brain stimulation, intracerebral grafts, direct brain injection, intrathecal brain delivery and so forth. Due to the huge risks and pains caused by the invasive approaches, people are turning more and more attention to the non-invasive approaches, which include receptor-mediated transcytosis, the use of neurotropic viruses, exosomes, nanoparticles and so on¹⁵⁻¹⁷. Among these non-invasive strategies, the nanoparticulate drug delivery systems have shown promising clinical value in GBM therapy due to their appealing properties such as high drug loading efficiency, spatial- and temporal-controlled drug release, real-time visualization during the therapeutic process and so forth¹⁸⁻²⁶. Despite these elegant works, there are still no clinically approved nanoparticle-based therapies against GBM owing to the following hurdles: (1) the intrinsic properties of nanoparticles such as size, surface charge and opsonization can influence uptake of them into phagocytes, thereby preventing them entry into the brain; (2) the premature

release of payload might occur during systemic circulation since therapeutic agents are generally loaded on nanoparticles through charge interaction or hydrophobic interaction; (3) the nanoparticles even crossing BBB still hardly penetrate deeply into GBM tissues owing to the high interstitial fluid pressure of GBM tissues, thus hampering their therapeutic effects^{5,15,27,28}.

On the other aspect, bacteria recently have achieved encouraging outcomes in cancer therapy^{29–33}. Conceptually, bacteria for cancer treatment are independent of ‘genetic makeup’, featuring superior merits over conventional treatments including intrinsic tumour navigation ability, tumour tissue-penetration ability as well as gene packaging ability. Remarkably, it has been well demonstrated that bacteria can cross the BBB transcellularly, paracellularly and/or in infected phagocytes^{34–36}, which is the basis of bacterial systems for the treatment of GBM. However, GBM therapies with live bacteria are still few, since they encounter numerous challenges, such as difficulty in precise control of drug release, inadequate stimulation to immune responses, and potential bacterial toxicity (e.g., bacteremia)^{35–37}. Intriguingly, there are increasing enthusiasms for developing bacteria-nanoparticles hybrid systems for the drug delivery against other types of cancer^{38,39}. However, in these systems, the nanoparticles are generally loaded on the surface of bacteria, and thus they still suffer from the afore-mentioned drawbacks often associated with free nanoparticles. Moreover, the surface loaded nanoparticles might break the integrity of the capsule of bacteria, and the intact capsule can prevent fusion of bacteria with lysosomes, which is necessary for traversal of the BBB as live bacteria^{34,40}. Taken together, bacteria-nanoparticles hybrid system across BBB for fighting GBM has not yet been achieved.

To this end, we herein develop a novel Trojan bacteria system to delivery therapeutics into brain for photothermal immunotherapy of GBM. The therapeutics are composed of glucose polymer (GP)-conjugated and indocyanine green (ICG)-loaded silicon nanoparticles (GP-ICG-SiNPs). The GP-ICG-SiNPs can be selectively and robustly internalized by the facultatively anaerobic bacteria (e.g., attenuated *Salmonella typhimurium* VNP20009 (VNP), *Escherichia coli* 25922 (EC)) through the bacteria-specific ATP-binding cassette (ABC) transporter to form the Trojan bacteria system. Compared with free therapeutics hardly entering the brain and penetrating GBM tissue, the constructed Trojan bacteria can take therapeutics together to across the BBB, target GBM and then penetrate the GBM tissue more deeply. Afterwards, under the irradiation of 808 nm laser, the PTT effects originated from ICG enable the destruction of tumour cells as well as the lysis of bacterial cells. These released tumour-associated antigens and bacterial debris would trigger antitumor immune responses. We demonstrate that the Trojan bacteria exhibit better therapeutic effects towards GBM compared with the pristine bacteria. We anticipate the proposed Trojan bacteria system will catalyze innovative therapies for various CNS diseases, and GBM treatment in the work only serve as an initial proof of principle.

Results

Design of Trojan bacteria system. The basic concept of Trojan bacteria is schematically shown in Fig. 1a. The nanoagents consist of three components: the core particle of SiNP, the bacteria-targeting ligand of

GP and the photothermal agent of ICG. As schematically illustrated in the synthetic route of GP-ICG-SiNPs (**Supplementary Fig. 1**), the GP molecules are firstly conjugated to the SiNPs surface based on the Schiff base reaction between the aldehyde groups of GP and the amino SiNPs⁴¹. After that, the ICG molecules are loaded on GP-SiNPs through electrostatic adsorption. The constructed nanoagents can selectively enter intracellular volume of bacteria (e.g., VNP, EC) to form Trojan bacteria system through the bacteria-specific ABC transporter pathway⁴²⁻⁴⁶. Fig. 1b schematically illustrates the Trojan bacteria serving as a carrier to deliver therapeutics to cross the BBB to achieve light-triggered combination therapy of GBM. In a typical experiment, after intravenous injection of Trojan bacteria, they could take the internalized therapeutics together to cross the BBB, and eventually target and penetrate GBM tissues. Under 808-nm irradiation, the ICG molecules loaded on SiNPs could convert light energy into the sufficient heat to lysis host bacterial cells and destruct tumour cells. As a result, a pool of tumour-associated antigens and bacterial residues could together promote antitumor immune responses⁴⁷⁻⁵¹. Typically, immature dendritic cells (iDCs) recognize tumour-associated antigens and bacterial residues through pattern recognition receptors and become mature DCs (mDCs). Meanwhile, mDCs migrate to lymphoid organs to express a large number of cytokines and stable major histocompatibility complex to activate T cells (TCLs). As a consequence, the TCLs express cytokines like TNF- α and IFN- γ , leading to a remarkable immune therapeutic outcome.

Characterization of Trojan bacteria system. A series of experiments were carried out to demonstrate the successful preparation of GP-ICG-SiNPs including transmission electron microscopy (TEM), dynamic light scattering (DLS), UV-vis absorbance (UV), photoluminescence (PL) and flow cytometry. As shown in the TEM image in **Supplementary Fig. 2**, GP-ICG-SiNPs appear as spherical particles with a narrow size distribution of ~ 4.1 nm, which is slightly larger than that of bare SiNPs (e.g., ~ 2.7 nm). The DLS spectra in **Supplementary Fig. 3** reveal the hydrodynamic diameter of GP-ICG-SiNPs is ~ 6.5 nm, also larger than the hydrodynamic diameter of bare SiNPs (~ 3.6 nm). As shown in **Supplementary Fig. 4a**, three distinct peaks located at 320 nm (assigned to SiNPs), 731 nm, and 790 nm (assigned to ICG) exist in the absorption spectrum of GP-ICG-SiNPs, confirming the successful loading of ICG molecules. As further revealed in **Supplementary Fig. 4b**, upon the treatment of phenol-sulfuric acid, the absorption spectrum of GP-ICG-SiNPs displays a new peak at 490 nm since the linked GP is hydrolyzed into furfural derivative, followed by the formation of furfural resin with phenol⁵². The new appearing peak confirms the successful conjugation of GP molecules. The amounts of linked GP and loaded ICG onto SiNPs can be quantified based on the corresponding calibration absorption curves (**Supplementary Fig. 5**), respectively. **Supplementary Figs. 6a and 6b** give the PL spectra of GP-ICG-SiNPs under the excitation of 405 nm or 780 nm, respectively. Typically, the two characteristic emission peaks located at 485 nm and 810 nm are respectively corresponding to SiNPs and ICG. The photothermal curves in **Supplementary Fig. 7** suggest that the temperature of GP-ICG-SiNPs solutions can be enhanced by 32°C during 300-sec 808-nm laser exposure when the loading concentration of ICG is or more than 150 $\mu\text{g}/\text{mL}$. These results together demonstrate the successful modification of ICG molecules with SiNPs.

To test the generality of the proposed Trojan bacteria strategy, two representative bacteria of VNP and EC were selected for the following experiments. The VNP or EC were incubated with the synthesized GP-ICG-SiNPs at 37 °C for 2 h, and then washed with phosphate buffered saline (PBS) buffer for several times. As revealed in the scanning electron microscope (SEM) images in Fig. 2a, the surface and the morphology of Trojan bacteria is similar to that of pristine bacteria. As further confirmed by elemental mapping in high-angle annular dark field-scanning transmission electron microscope (HAADF-STEM) images (Fig. 2b), the silicon element exists only in Trojan EC or Trojan VNP rather than in pure EC or VNP. SEM and TEM images together prove that the prepared therapeutics indeed enter bacteria rather than nonspecifically absorb on the bacterial surface. Moreover, Trojan bacteria have the same growth curve compared with the untreated bacteria (**Supplementary Fig. 8a**), and their survival rate could maintain as high as 90% or more (**Supplementary Fig. 8b**), indicating the growth and activity of host bacteria would not be greatly influenced by the internalized therapeutics.

As shown in the confocal laser scanning microscope (CLSM) images in Fig. 2c, the green fluorescence from SiNPs (first column, $\lambda_{\text{ex}} = 405 \text{ nm}$, $\lambda_{\text{em}} = 500\text{-}550 \text{ nm}$) and the red fluorescence from ICG (second row, $\lambda_{\text{ex}} = 633 \text{ nm}$, $\lambda_{\text{em}} = 700\text{-}800 \text{ nm}$) could be simultaneously observed in the Trojan bacteria. On the contrary, no fluorescent signals are detected when EC or VNP are treated with ICG-SiNPs under the same conditions (Fig. 2d). Quantitatively, the uptake efficiency of nanoagents by EC or VNP cells was further determined by flow cytometry. As revealed in Fig. 2e, the uptake efficiency of GP-ICG-SiNPs by EC or VNP after 2 h of incubation is gradually rising when increasing the concentration of GP-ICG-SiNPs. Typically, when the GP-ICG-SiNPs is 10 mg/mL, the uptake efficiency is 56.8% for EC and 50.5% for VNP. If further enhancing the concentration to 15 mg/mL, the uptake efficiency does not improve significantly, e.g., 62.1% for EC and 55.7% for VNP. As such, 10 mg/mL GP-ICG-SiNPs is employed in the following experiments.

We further performed inhibition assay and competition assay to confirm whether GP-ICG-SiNPs entering bacteria was through the ABC transporter pathway. For the inhibition assay, no fluorescent signals are measured when EC or VNP are co-incubated with sodium azide (NaN_3) and GP-ICG-SiNPs, in which NaN_3 serves as the inhibitor of ABC transporter (**Supplementary Fig. 9**)⁵³. For the competition assay, EC or VNP were first incubated with 0, 5 and 20 mg/mL of GP and then incubated with GP-ICG-SiNPs. As indicated in **Supplementary Fig. 10**, the fluorescence of bacteria becomes gradually weakened with the increase of GP concentrations. To testify the selectivity of GP-ICG-SiNPs for bacteria over mammalian cells, the mixture of human blood and bacteria were incubated with GP-ICG-SiNPs for 2 h. As shown in Fig. 2d and **Supplementary Fig. 11**, fluorescence signals are only observed in EC or VNP rather than in red blood cells (RBCs). These results together demonstrate that GP-ICG-SiNPs can be internalized into bacteria to form the Trojan system *via* the bacteria-specific ABC transporter pathway.

Trojan bacteria against tumour *in vitro*. We next studied the photothermal ability of Trojan bacteria. Under 808-nm laser irradiation, the constructed Trojan bacteria (Trojan EC or Trojan VNP) could heat up to 55°C within 400 s, slightly lower than the temperature achieved by the equivalent free GP-ICG-SiNPs (Fig. 3a).

Accordingly, the bacterial cell viability gradually decreases as the temperature increases from 48 to 55 °C (Fig. 3b). In particular, the bacterial cell viability is only 37% at 52 °C. Meanwhile, the overall morphology of the Trojan bacteria begins to rupture when the temperature rises to 48 °C, as shown in the SEM image in Fig. 3c. These results manifest that the constructed Trojan bacteria feature good photothermal activity.

Next, we investigated whether the photothermal effects produced by the Trojan bacteria could destroy glioblastoma G422 cells. In live-dead cell staining, the red fluorescence is only observed in most of Trojan bacteria-treated G422 cells (Fig. 3d). In MTT assay, under the irradiation of 808 nm for 5 min, the cell viability of G422 cells dramatically decreases to less than ~20% when they are incubated with Trojan bacteria or equivalent free GP-ICG-SiNPs for 6 h, much lower than the 100% of other control groups ($p < 0.001$) (Fig. 3e).

In the constructed Trojan bacteria system, tumour-associated antigens and bacterial residues produced by PTT might trigger an effective immune response. To testify this hypothesis, we designed a transwell system to study this effect *in vitro*. As shown in the Fig. 3f, G422 cells with different treatments are placed in the upper chamber of the transwell system, and DCs are seeded in the lower chamber. After that, the maturation of DCs are evaluated by flow cytometry. The up-regulation of co-stimulatory factors CD80 and CD86 as the typical markers on the surface of DCs indicate the level of DCs maturation^{54,55}. As revealed in Figs. 3g-3h, compared with the control groups, the level of DCs maturation can be significantly improved when G422 cells were treated with Trojan bacteria system under 808-nm irradiation (e.g., 60.6% DC maturation in Trojan EC group, 64.8% DC maturation in Trojan VNP group). These results indicate that the tumour-associated antigens and bacterial residues produced by PTT could trigger effective DC maturation.

In vivo behaviors of bacteria in mice. Before cancer treatment, we have systematically studied the behavior of bacteria in mice after tail vein injection. We first determined the safe dose of bacteria injected into the mice. The body weights were measured for healthy mice injected with EC or VNP at $\sim 1 \times 10^6$, $\sim 1 \times 10^7$ and $\sim 1 \times 10^8$ CFU (Fig. 4a). Specially, at the high dose of $\sim 1 \times 10^8$ CFU EC or VNP, the mouse body weights rapidly dropped, and one or two of five mice died respectively in the EC or VNP-treated groups, implying the severe toxicity of bacteria at such a high dose. Under lower doses, i.e., $\sim 1 \times 10^6$ and $\sim 1 \times 10^7$ CFU per mouse, the mouse body weights did not change significantly, and no mice died in the corresponding group. Therefore, EC or VNP at a moderate dose ($\sim 1 \times 10^7$ CFU per mouse) with a tolerable side effect were employed in the following experiments.

To reveal the *in situ* and real-time location of bacteria *in vivo*, we transformed the pRSETB-mCherry plasmids into EC (mCherry@EC) or VNP (mCherry@VNP) to express red fluorescence protein of mCherry (**Supplementary Fig. 12**). Afterwards, the female health Balb/c mice were injected with these engineered VNP or EC through the tail vein at the dose of $\sim 1 \times 10^7$ CFU per mouse. The mice were then sacrificed at 12, 24, 72, 120 and 360 hours after intravenous injection to obtain their main organs (e.g., brain, heart, liver, spleen, lung and kidney), followed by the detection of red fluorescence of mCherry by an *in vivo*

optical imaging system (IVIS Lumina III). As shown in Figs. 4b-4d, the fluorescence signal mainly exists in the liver, and is gradually weakened over time, which is basically undetectable at 15 days. We then homogenized the extracted organs, serially diluted (10-fold), and plated them on solid LB agar plates. In consistent with the results of *ex vivo* images, bacteria mainly accumulated in the liver and were quickly cleared from all extracted organs. The total elimination was basically achieved at 15 days (Figs. 4e-4g).

To further ensure the safety of bacterial injection, routine blood tests including complete blood and serum biochemical analysis were performed on the tested dose, i.e., $\sim 1 \times 10^7$ CFU per mouse (Figs. 4h-4q). Compared with untreated healthy mice, all serum biochemical parameters and most blood routine data were within the normal range at the first day of bacterial injection, except for a decrease in white blood cell (WBC) and platelet count. At the fifth day of bacterial injection, the WBC count and platelet count of the bacteria-treated mice returned to normal ranges, indicating that the acute inflammation caused by EC and VNP infection was mild and tolerated by the mice and did not develop chronic toxicity within 5 days.

Trojan bacteria crossing BBB, targeting and penetrating glioblastoma. Next, we performed a series of experiments to demonstrate the constructed Trojan bacteria could cross the BBB. We first built an *in vitro* human brain microvascular endothelial cell (HBMEC) model to investigate whether the Trojan bacteria could cross the BBB (Fig. 5a)^{56,57}. The construction of HBMEC model was evaluated by the measurement of transepithelial electrical resistance (TEER) (**Supplementary Fig. 13a**). Experimentally, Trojan bacteria were inoculated with HBMEC cells in the upper chamber (apical chamber) of transwell at a dose of $\sim 8 \times 10^4$ CFU/well, followed by collecting 10 μ L of culture medium from the lower chamber at 1h, 2h, 3h and 4h, respectively. The penetration rate of Trojan bacteria crossing the BBB was determined by counting the number of colonies on the LB solid medium the next day (**Supplementary Fig. 13b**). As revealed in Fig. 5b, the penetration rate of EC and VNP increases gradually with time, climbing to 49.7% and 60% at 4h, respectively. These results demonstrate the Trojan bacteria can cross the BBB in the *in vitro* model.

Afterwards, the female Balb/c mice with *in situ* GBM were injected with these mCherry@VNP or mCherry@EC through the tail vein at the dose of $\sim 1 \times 10^7$ CFU per mouse. As revealed in *ex vivo* images in Figs. 5c- 5e, the red fluorescence of bacteria could be found in GBM after 12 h of bacteria injection, gradually increasing following the time. By contrast, the fluorescence from bacteria in other organs like liver decreases exponentially following the time. Such difference might be resulted from the selective proliferation of bacteria in the hypoxic, immunosuppressive, and biochemically unique glioblastomas microenvironment^{33,58-60}. And through the results of the plates, the amount of EC or VNP in brain counted in each plate was much higher than that in other organs. Specifically, the CFU of bacteria in brain reached its peak up to $\sim 0.51 \times 10^6$ CFU/g for EC and $\sim 0.74 \times 10^6$ CFU/g for VNP at the 120 h post-injection with bacteria (Figs. 5f- 5h).

With an aim to study the intratumoural transport of constructed system, we first constructed an *ex vivo* model of three dimensional cultured multicellular spheroids (MCSs), which were made of U87MG cells when the diameter of MCSs arrived at $\sim 750 \mu$ m. PBS, GP-ICG-SiNPs (8 mg/kg ICG), mCherry@VNP

($\sim 1.0 \times 10^7$ CFU) and Trojan bacteria (GP-ICG-SiNPs (8 mg/ml ICG) internalized into $\sim 1.0 \times 10^7$ CFU mCherry@VNP) were co-incubated with U87MG MCSs for 12h, respectively. Fluorescence signals at different depths of MCSs were collected by CLSM. The three-dimensional confocal images show that the MCSs treated by Trojan bacteria display distinct green (from SiNPs) and red (from mCherry@VNP) fluorescence signals at both the edge and internal space, with a penetration depth of $\sim 260 \mu\text{m}$ (Fig. 5i). In addition, the distribution of Trojan bacteria in MCSs is basically consistent with that of pure mCherry@VNP, but much deeper than that of free GP-ICG-SiNPs. These results indicate that the constructed Trojan bacteria could penetrate deep GBM tissues *in vitro*.

To verify the constructed Trojan bacteria could penetrate the deep GBM tissues *in vivo*, the female Balb/c mice with *in situ* GBM were intravenously injected with PBS, GP-ICG-SiNPs, EC, VNP, Trojan EC or Trojan VNP, respectively. Afterwards, the excision and section of deep GBM tissue was performed at 12 h post injection, followed by hypoxia inducible factor- α (HIF- α) analysis and the bacterial 16S RNA fluorescence *in situ* hybridization (FISH) analysis. The expression level of HIF- α indicates the hypoxia situation in GBM tissues and the expression of 16S RNA indicates the location of injected bacteria in GBM tissues. As revealed in Fig. 5j, we can observe distinct green fluorescence signal of HIF- α in all groups, suggesting the high hypoxia level of deep GBM tissues. In addition, the distinct red fluorescence signals of 16S RNA are only found in EC, VNP, Trojan EC and Trojan VNP-treated groups, suggesting Trojan bacteria with hypoxia-targeting ability indeed penetrate GBM tissues *in vivo*.

Trojan bacteria-induced photothermal immunotherapy. Based on the proven ability of Trojan EC and Trojan VNP to cross the BBB, target and penetrate GBM, we next investigated the photothermal immune efficacy of Trojan bacteria in the treatment of orthotopic GBM-bearing mice. As schematically illustrated in Fig. 6a, the orthotopic tumour model was constructed by *in situ* inoculation of $\sim 8 \times 10^5$ Luc-G422 cells per mouse at day -7. At day 0, the tumour-bearing mice were divided into six groups, including intravenous injection of (G1) PBS, (G2) $\sim 1 \times 10^7$ CFU EC, (G3) $\sim 1 \times 10^7$ CFU VNP, (G4) GP-ICG-SiNPs (8 mg/kg ICG), (G5) Trojan EC (e.g., GP-ICG-SiNPs (8 mg/kg ICG) internalized into $\sim 1 \times 10^7$ CFU EC) and (G6) Trojan VNP (e.g., GP-ICG-SiNPs (8 mg/kg ICG) internalized into 1×10^7 CFU VNP).

The fluorescence signals of ICG can be employed for monitoring the dynamic distribution of GP-ICG-SiNPs as well as Trojan bacteria in the body. **Supplementary Fig. 14** shows the fluorescence signals of ICG in the brain peaked at ~ 12 -hour post-injection of Trojan bacteria. Therefore, at the 12-hour post-injection of Trojan bacteria, the brains of those mice were suffered by an 808 nm irradiation ($1.2 \text{W}/\text{cm}^2$, 5 min). As revealed in the photothermal images record by an IR camera (Fig. 6b), the rapid GBM temperature rising only occurs in Trojan EC or Trojan VNP-treated groups. In particular, the GBM-surface temperature can increase to $50.7 \text{ }^\circ\text{C}$ in Trojan EC group after 5-min irradiation, and $51.7 \text{ }^\circ\text{C}$ in Trojan VNP group after 5 min irradiation (Fig. 6c). By contrast, significant heating is not observed in other control groups under the same conditions. Next, at 5-day and 10-day post-injection, GP-ICG-SiNPs, Trojan EC, Trojan VNP at the same dose were intravenously injected into the mice again. Analogously, at 5-day and 12-hour post-injection or 10-day and 12-hour post-injection, the GBM sites of these mice were irradiated

by 808 nm laser and the temperature of GBM sites was stabilized at 50°C for 5 min by adjusting the 808 nm laser power. Afterwards, bioluminescence imaging was applied to visualize the anti-tumor effect every four days. As displayed in Figs. 6d-6e, the bioluminescence signals of luc-G422 cells in Trojan EC or Trojan VNP groups are much weaker than that of the other treatment groups. The quantitative analysis shows that Trojan bacteria system has obvious inhibitory effect on tumour growth, and the corresponding inhibition rates are 66.25% of Trojan EC and 70.11% of Trojan VNP, respectively, which are much better than 16.14% of EC, 11.88% of VNP and 8.01% of GP-ICG-SiNPs (Fig. 6f). Also, survival analysis shows that survival time of mice has been significantly prolonged in Trojan bacteria group compared with other control groups (Fig. 6g). To further evaluate the antitumor effects of Trojan bacteria system, H&E staining of GBM tissues were performed. As shown in Fig. 6h, the most apparent tumour cell destruction, tissue necrosis and nuclear pyknosis are found in Trojan bacteria-treated group. Taken together, these therapeutic data demonstrated the adaptable anticancer ability of Trojan bacteria *in vivo*.

As previously reported, the lysates of tumour and bacterial cells can function as tumour vaccines and initiate tumour-specific immune responses^{33,61}. Hence, the *in vivo* DCs maturation triggered by Trojan bacteria system was evaluated. On the third day of the last treatment, we harvested the carotid lymph nodes and homogenized them into single cell suspensions. After staining with fluorophore labeled anti-CD11c, anti-CD86 and anti-CD80 antibodies, the cell suspensions were collected for flow cytometry analysis. As shown in Figs. 6i and 6j, compared with control groups, the highest level of DC maturation was observed in the groups of Trojan bacteria+laser (e.g., 39.4% DC maturation for Trojan EC, 42.7% DC maturation for Trojan VNP), which could be attributed to the release of tumor-associated antigens and bacterial residues upon photothermal effect. On the other aspect, splenocytes from each group were co-stained with anti-CD3, anti-CD4 and anti-CD8a antibodies, and the percentage of CD3⁺ CD8a⁺ T cells was measured by flow cytometry. As shown in **Supplementary Fig. 15** and Fig. 6k, no significant difference on CD8a⁺ T cell response was observed between GP-ICG-SiNPs group (21.2%) and PBS control (19.8%). On the contrary, the percentage of CD8a⁺ T cells in splenocytes after the combined photothermal ablation with Trojan EC treatment (30.6%) and Trojan VNP treatment (34.1%) were much higher than that of EC (27.3%) and VNP (26.3%) with laser irradiation. At the same time, we assessed the percentage of CD3⁺ CD8a⁺ T cells in the tumours by flow cytometry. As revealed in **Supplementary Fig. 16** and Fig. 6l, no significant difference on CD8a⁺ T cell response was observed between GP-ICG-SiNPs group (8.31%) and PBS control (7.06%). On the contrary, the percentage of CD8a⁺ T cells in splenocytes after the combined photothermal ablation with Trojan EC treatment (19.1%) and Trojan VNP treatment (22.4%) were much higher than that of EC (10.8%) and VNP (11.4%) with laser irradiation. In addition, we also evaluated the cytokine levels of TNF- α and IFN- γ in serum samples of mice after various treatments. In the cytokine assay of serum samples, levels of both cytokines (IFN- γ and TNF- α) were higher in mice treated with Trojan bacteria than those in mice treated with pure bacteria and nanoagents (Figs. 6m and 6n). The increasing TNF- α and IFN- γ levels combined with the elevation of the percentage of CD8a⁺ T cells further confirm the boosted immunity in the mice injected with Trojan bacteria under laser irradiation.

The elimination of residual bacteria after photothermal immunotherapy. Next, we examined whether the photothermal immunotherapy induced by Trojan bacteria could facilitate the elimination of bacteria from the GBM-bearing mice. In detail, the GBM-bearing mice were intravenously injected with (G1) PBS, (G2) $\sim 1 \times 10^7$ CFU mCherry@EC, (G3) $\sim 1 \times 10^7$ CFU mCherry@VNP, (G4) Trojan mCherry@EC (e.g., GP-ICG-SiNPs (8 mg/kg ICG) internalized into $\sim 1 \times 10^7$ CFU mCherry@EC) or (G5) Trojan mCherry@VNP (e.g., GP-ICG-SiNPs (8 mg/kg ICG) internalized into 1×10^7 CFU mCherry@VNP), respectively. At the 12-hour post-injection, the brains of those mice were suffered by an 808 nm irradiation (1.2 W/cm^2 , 5 min), followed by *ex vivo* imaging of the main organs at 5-day post-injection. As shown in Figs. 7a and 7b, relatively strong red fluorescence signals of mCherry could be detected in GBMs and livers in G2-G5 groups. Of note, the fluorescence intensity in the Trojan bacteria treatment groups (G4 and G5) is significantly lower than that in pure bacteria treatment groups (G2 and G3). These findings are further confirmed by major organs and GBM tissues harvesting, homogenization and then culturing the homogenates on plates (Figs. 7c and 7d). It is found that sporadic colonies grew from homogenates of GBM and livers in the Trojan bacteria treatment groups (G4 and G5), much less than those in pure bacteria treatment groups (G2 and G3). Accumulating evidence demonstrated only Trojan bacteria-treated mice under NIR irradiation could help to eliminate bacteria from the body.

Discussion

Due to the existence of the BBB in GBM, the accumulation of peripherally administered drugs into brain is seriously hindered. It has been reported that bacteria can bypass the BBB transcellularly, paracellularly and/or in infected phagocytes³⁴⁻³⁶. Intriguingly, cancer therapeutics internalized into bacteria would potentially circumvent drug delivery issues in GBM therapy. However, this progress is still in its infancy due to the lack of a natural connection between therapeutics and the microbiome. Herein, the developed Trojan bacteria system naturally bridge the divide between therapeutics and bacteria. We have previously demonstrated that bacteria including Gram-negative as well as Gram-positive bacteria actively swallowed GP-conjugated nanoparticles through bacteria-specific ABC transporter pathway for ultrasensitive diagnosis of bacterial infections⁴². In this context, we have successfully constructed Trojan bacteria as drug delivery vehicles for GBM therapy, in which the Trojan bacteria system was made of GP-ICG-SiNPs internalized into VNP or EC. Consistently with previous reports, the as-prepared GP-ICG-SiNPs could be internalized into the host bacteria, confirmed by TEM, SEM and confocal images. We also performed an inhibition assay as well as a competition assay to further verify GP-ICG-SiNP accessing into the bacterial intracellular volume was through the ABC transporter pathway.

Subsequently, we demonstrated the notion that the constructed Trojan bacteria could cross BBB, target and penetrate GBM. As such, in the constructed Trojan bacteria, the bacteria could take therapeutics together to cross BBB, target and penetrate GBM tissues. Consequently, under the irradiation of 808-nm laser, photothermal treatment of ICG can induce tumour cell destruction and bacterial rupture. The produced lysates of tumour and bacterial cells upon PTT effects can act as immune stimulants to enhance the anti-tumor immune response. Compared with the use of equivalent free GP-ICG-SiNPs or

pure bacteria for GBM therapy, this constructed Trojan bacteria system not only greatly augmented targeted delivery of GP-ICG-SiNPs towards the GBM, but also synergistically promoted antitumor immune responses that prolonged the survival of GBM-bearing mice. In addition, distinguished from pure bacteria therapy which would preserve a lot of residual bacteria after treatment, that residual bacteria could be effectively eliminated from the body after the Trojan bacteria treatment. Accumulating evidence demonstrated that the therapeutic system of Trojan bacteria could achieve photothermal immunotherapeutic effects and safety profiles under modulation of NIR light irradiation, providing a plausible microbiota-based therapeutic strategy against CNS diseases.

Methods

Synthesis of GP-ICG-SiNPs. SiNPs were synthesized by mixing 1,8-naphthalimide and 3-aminopropyltrimethoxysilane, followed by 365 nm UV irradiation at room temperature for 40 min. The resulted solution was then centrifuged at 6000 rpm for 20 min to remove unreacted reagents, and further purified by dialysis (MWCO, 1000, Spectra/Pro). The as-synthesized SiNPs (200 μ L, 20 mg/mL) were mixed with GP (100 μ L, 10 mg/mL) at 70 $^{\circ}$ C for 6 h, followed by the addition of 0.02 mg of NaBH₄. After reacting 12 h at room temperature, the stable GP-modified SiNPs were obtained. To remove unreacted GP, Nanosep centrifugal devices (MW cutoff, 3 kDa; Millipore) were used to filter the reaction solution at 7500 rpm for 15 min. After that, ICG were co-incubated with GP-SiNPs, and stirred at 4 $^{\circ}$ C overnight. Then, the unreacted ICG were centrifuged by Nanosep centrifugal devices (MW cutoff, 3 kDa; Millipore) at 7000 rpm for 15 min. Then the products of GP-ICG-SiNPs were harvested and stored at 4 $^{\circ}$ C in the dark for the following experiments. Transmission electronic microscopy (TEM, Philips CM 200) with 200 kV was used for the characterization of the morphology and size of the nanoagents. UV-vis absorption spectra of nanoagents were measured by A 750 UV-vis near-infrared spectrophotometer (Perkin-Elmer lambda). Photoluminescence (PL) spectra of nanoagents were recorded by a spectro-fluorimeter (HORIBA JOBIN YVON FLUORMAX-4). Dynamic light scattering (DLS) of nanoagents was analyzed by a Delsa™ nano submicron particle size analyzer (Beckman Coulter, Inc).

Bacterial culture. Attenuated *Salmonella* strain VNP20009 (VNP) and *Escherichia coli* 25922 (EC) were purchased from American Type Culture Collection (ATCC). These bacterial cells were harvested at the exponential growth phase when they were cultured in LB liquid medium (250 rpm, 37 $^{\circ}$ C). Afterwards, the bacterial suspensions were washed twice and re-suspended in PBS buffer for the following experiments. The bacteria count in solution was determined by the measurement of corresponding optical density (OD) at 600 nm. The numbers of bacterial colonies were counted by a colony counting instrument (Czone 8).

Construction of mCherry@VNP and mCherry@EC. To construct mCherry@VNP, monoclonal VNP was selected and inoculated in 2 mL of LB liquid medium without ampicillin. Then, 0.5 mL of bacterial solution was added into 50 mL LB liquid medium and cultured at 37 $^{\circ}$ C until its OD₆₀₀ reached 0.5. After that, the shake flask was ice-bathed for 30 min, and 25 mL of bacterial solution was added to a pre-

cooled 50 mL round bottom centrifuge tube, and centrifuged at 4 °C and 1000 rpm for 15 min to obtain bacterial pellets. Then the bacterial precipitation was washed twice with pre-cooled sterile water. The bacterial pellet was resuspended with 10 mL of 10% sterile glycerin, and centrifuged at 4 °C and 1000 rpm for 15 min. Then 50 μ L 10% sterile glycerin was added to make the bacterial precipitation fully suspended and transferred to a precooled 0.5 mL centrifuge tube to form electrically transformed competent cells. We took 1 ng of mCherry plasmid and added it to VNP competent cells, mixed it gently, ice bath for 1 min, transferred it into a cold electroporation cup (Bio-Rad), and placed it on the electrode for electric shock transformation (Electric shock parameter: voltage = 2.5 kV, capacitance = 25 μ F, resistance = 200 Ω). After the electric shock, we added immediately 1 mL of LB liquid medium to the electroporation cup, mixed, and transferred all to a sterile 1.5 mL centrifuge tube, let it cultured at 30 °C and 160 rpm for 1.5 h. Then, we took about 200 μ L of bacterial solution and plated it on solid LB agar containing ampicillin, and incubated the LB solid plate at 37 °C until a single colon is formed. To construct mCherry@EC, we added 1 ng mCherry plasmid to 100 μ L of EC competent bacteria, and iced bath for 30 min. Then the bacteria liquid was heat shocked at 42 °C for 90 s, and then ice bathed for 2 min. The bacterial cells were added with 900 μ L LB liquid medium without ampicillin and cultured at 180 rpm at 37 °C for 45 min. To obtain the bacterial precipitation, the bacterial solution was centrifuged at 6000 rpm for 5 min, and about 100 μ L supernatant was retained for mixing. Pipette 100 μ L of the resuscitated bacterial solution evenly on the LB solid plate containing ampicillin. Afterwards, the plate was cultured upside down in an incubator for 12 to 16 h at 37 °C.

Construction of Trojan bacteria. The 20 μ L of VNP or EC suspension with $\sim 1.0 \times 10^7$ CFU was purified and resuspended, followed by incubation with GP-ICG-SiNPs (15 mg/mL, 200 μ L) in a shaking incubator at 200 rpm, 37 °C for 2 h. The constructed Trojan bacteria were harvested by centrifugation at 8000 rpm for 10 min. Afterwards, the harvested Trojan bacteria were re-suspended again and washed with PBS buffer at least 3 times to remove excess GP-ICG-SiNPs or non-specifically absorbed GP-ICG-SiNPs. To characterize the constructed Trojan bacteria, the solution containing Trojan bacteria of 10 μ L was transferred onto a microscope slide and covered by a coverslip, followed by confocal laser scanning microscope imaging (CLSM, Leica, TCSSP5 II) with 30% power of diode laser. Of note, all fluorescent images were captured under identical optical conditions. The processing and analysis of the region of interest (ROI) were performed by the image analysis software (Leica Application Suite Advanced Fluorescence Lite). The morphology and structure of Trojan VNP and Trojan EC were characterized by TEM and SEM.

Cellular experiments in vitro. The G422 mouse glioblastoma cell line was obtained from Shanghai Zhong Qiao Xin Zhou Biotechnology and cultured under appropriate conditions. Dendritic cells (DCs) were isolated from the bone marrow of female Balb/c mice about 6-8 weeks old. G422 cells were inoculated in a 96-well plate, co-incubated with EC, VNP, GP-ICG-SiNPs Trojan EC or Trojan VNP for 6 h, irradiated with or without 808-nm laser for 5 min, and then cleaned with sterile PBS. MTT assay was used to determine the cellular viability. On the other aspect, the treated cells were stained with Calcein-AM (CAM) and propidium iodide (PI), and then analyzed by confocal microscopy (CAM: λ_{ex} = 488 nm, λ_{em} = 500-545 nm;

PI: $\lambda_{\text{ex}} = 543 \text{ nm}$, $\lambda_{\text{em}} = 560\text{-}620 \text{ nm}$). In order to evaluate the maturation of DCs *in vitro*, we designed a transwell system. The DCs in the lower chamber were collected, stained with anti-CD11c-FITC, anti-CD86-PE and anti-CD80-APC, and sorted by flow cytometry.

Human brain microvascular endothelial cell model. A 12-well transwell plate with 2 μm of mean pore size membrane was used to construct the *in vitro* human brain microvascular endothelial cell (HBMEC) model. The HBMEC cells (1.0×10^5 cells/well) were seeded in the transwell insert with 12 mm diameter. The transendothelial electrical resistance (TEER) values were detected by a Millicell-ERS volt-ohmmeter to monitor the cell monolayer integrity during the cell culture process. A TEER value between 150 and 300 $\Omega \text{ cm}^2$ was suitable for the further experiments.

Multicellular spheroids model. The 3D tumour spheroids of U87MG cells were obtained using a liquid overlay method. Each well of 96-well plates was pre-coated with 100 μL of the FBS free medium containing sterile agarose (2%, w:v). Subsequently, U87MG cells (5000 cells/well) were seeded into each well and cultured in the medium containing FBS (10%, v:v). The tumour spheroids were allowed to grow up to attain the diameter about 750 μm for 8 days at 37°C. The Z-stack scanning was performed on the U87MG multicellular spheroids from top to bottom with 40 μm per section by CLSM.

Animal experiments. All animal experimental procedures were performed according to the Guideline for Animal Experimentation with the approval of the animal care committee of Soochow University. In addition, the studies in human blood were conducted under a protocol that was reviewed and approved by the ethics committee of Soochow University. To construct the GBM-bearing mice model, the G422 cells (8×10^5 /per mouse) in a 5 mL volume were stereotactic injected using a 10 mL Hamilton syringe into the left striatum over 1 min into the following coordinates: 0.5 mm anterior, 2 mm left lateral from bregma, and 3.1 mm deep. To study the *in vivo* distribution of bacteria, mCherry@EC or mCherry@VNP ($\sim 1.0 \times 10^7$ CFU per mouse) was intravenously injected into the healthy mice or GBM-bearing mice after inoculation with Luc-G422 cells (10^5 /per mouse) for 7 days. Afterwards, the mice were sacrificed at specific time points (12, 24, 36, 72 and 120 h). Accordingly, the organs including heart, liver, spleen, lung and kidney as well as brain were extracted, followed by imaging *via* an *in vivo* optical imaging system (IVIS Lumina III). Meanwhile, the excised organs were homogenized in sterile PBS, in which the suspension solution was collected from the tissue dispersions by centrifugation at 1000 rpm to remove tissue fragments. Finally, the collected suspension solution was diluted by PBS buffer and cultured on LB solid medium at 37°C for 12 h, followed by counting bacterial colonies with a colony counting instrument (Czone 8). On the other aspect, the GBM-bearing mice were respectively injected with (G1) PBS, (G2) $\sim 1 \times 10^7$ CFU EC, (G3) $\sim 1 \times 10^7$ CFU VNP, (G4) GP-ICG-SiNPs (8 mg/kg ICG), (G5) Trojan EC (e.g., GP-ICG-SiNPs (8 mg/kg ICG) internalized into $\sim 1 \times 10^7$ CFU EC) and (G6) Trojan VNP (e.g., GP-ICG-SiNPs (8 mg/kg ICG) internalized into 1×10^7 CFU VNP) after inoculation for 7 days ($n=5$, female, 6-7 weeks old). After intravenous injection for 12 h, the GBM sites were irradiated by 808-nm laser (1.2 W/cm^2 , 5 min). The laser spot was adjusted according to the burr hole on the skull. The temperature of GBM sites was stabilized at 50°C for 5 min by adjusting the 808 nm laser power. Next, at 5-day and 10-day post-injection with bacteria, GP-ICG-SiNPs

(containing 8 mg/kg of ICG), Trojan EC, Trojan VNP were intravenously injected into the mice again. Analogously, at 5-day and 12-hour post-injection or 10-day and 12-hour post-injection, the GBM sites of these mice were irradiated by 808 nm laser and the temperature of GBM sites was stabilized at 50°C for 5 min by adjusting the 808 nm laser power. Afterwards, bioluminescence imaging was applied to visualize the anti-tumor effect every four days. On the other aspect, we harvested the carotid lymph nodes after 3 days post-last injection and homogenized them into single cell suspensions. Lymphocytes were stained with anti-CD11c-FITC, anti-CD80-APC and anti-CD86-PE for DC maturation analysis, while splenocytes labeled with anti-CD3-FITC anti-CD4-APC and anti-CD8a-PerCP was used to examine CD8a⁺ T cell response. Then, the mice were sacrificed at 16-day. GBM were harvested, and of which single cell suspensions were labeled with CD3-FITC and CD8a-PerCP was used to examine CD8a⁺ T cell response by flow cytometry. Meanwhile, serum samples were isolated from mice after various treatments and diluted for analysis. What's more, the tumors were harvested, fixed in 4% paraformaldehyde for 24 h, and embedded in paraffin. Tissues were sectioned, stained with H&E and then observed with an optical microscope. To examine whether residual bacteria were eliminated from the body after treatment, the excised organs after cancer treatment were imaged by the *in vivo* optical imaging system (IVIS Lumina III). Meanwhile, the harvested organs were homogenized in sterile PBS and the residual bacterial dispersions were collected by centrifugation. Then the collected bacterial solutions were diluted and cultured on an agarose medium for 12 h. The numbers of bacterial colonies were obtained by a colony counting instrument (Czone 8).

Statistical analysis. The confocal images were processed by the commercial image analysis software (Leica Application Suite Advanced Fluorescence Lite, LAS AF Lite) and common software of ImageJ (NIH Image; <http://rsbweb.nih.gov/ij/>). Error bars represent the standard deviation obtained from three independent measurements. All the statistical analyses were performed using the Origin and GraphPad Prism 7 software. The statistical significance of differences was determined by a one-way ANOVA analysis. $p < 0.05$ (*), $p < 0.01$ (**) and $p < 0.001$ (***) were used to indicate statistical difference.

Reporting Summary. Further information on research design is available in the Nature Research Reporting Summary linked to this article.

Declarations

Data availability. The main data supporting the results in this study are available within the paper and its Supplementary Information. The raw and analyzed datasets generated during the study are too large to be publicly shared, but are available for research purposes from the corresponding author on reasonable request.

Acknowledgements

We thank Dr. Liangzhu Feng (Soochow University, China) and Dr. Fei Peng (Harvard University, USA) for their general help and valuable suggestions. The authors acknowledge financial support from National

Natural Science Foundation of China (No. 21825402 and 22074101), Natural Science Foundation of Jiangsu Province of China (No. BK20191417), the China Postdoctoral Science Foundation (No. 2021M692347) and the Program for Jiangsu Specially-Appointed Professors to the Prof. Yao He, a project funded by the Priority Academic Program Development of Jiangsu Higher Education Institutions (PAPD), 111 Project as well as the Collaborative Innovation Center of Suzhou Nano Science and Technology (NANO-CIC).

Author Contributions

R. S., M. Z. L., H. Y. W. and Y. H. conceived and designed the research. R. S., and M. Z. L. carried out most of experiments and analyzed the data. J. P. L., B. B. C., Y. M. Y, and B. S. performed additional experiments and characterizations. R. S, and H. Y. W wrote the manuscript.

Competing interests

The authors declare no competing interests.

Additional information

Supplementary is available in the online version of the paper.

Supplementary Information is available in the online version of the paper.

Reprints and permissions information is available online at www.nature.com/reprints.

Correspondence and request for materials should be addressed to H. Y. W. or Y. H.

Publisher's note: Springer Nature remains neutral with regard to jurisdictional claims in published maps and institutional affiliations.

References

1. Purow, B., Schiff, D. Advances in the genetics of glioblastoma: are we reaching critical mass? *Nat. Rev. Neurol.* **5**, 419–426 (2009)
2. Stupp, R.; Mason, W. P.; Van den Bent, M. J. *et al.* Radiotherapy plus concomitant and adjuvant temozolomide for glioblastoma. *N. Engl. J. Med.* **352**, 987–996 (2005).
3. Yamaguchi, S.; Motegi, H.; Ishi, Y. *et al.* Clinical outcome of cytoreductive surgery prior to bevacizumab for patients with recurrent glioblastoma: a single-center retrospective analysis. *Neurol.*

- Med Chir.* **61**, 245–252 (2021).
4. Weller, M., Wick, W., Aldape, K. et al. Glioma. *Nat. Rev. Dis. Primers* **1**, 15017 (2015).
 5. Wu, L.P., Ahmadvand, D., Su, J. et al. Crossing the blood-brain-barrier with nanoligand drug carriers self-assembled from a phage display peptide. *Nat. Commun.* **10**, 4635 (2019).
 6. Gasca-Salas, C., Fernández-Rodríguez, B., Pineda-Pardo, J.A. et al. Blood-brain barrier opening with focused ultrasound in Parkinson's disease dementia. *Nat. Commun.* **12**, 779 (2021).
 7. Xue, J., Zhao, Z., Zhang, L. et al. Neutrophil-mediated anticancer drug delivery for suppression of postoperative malignant glioma recurrence. *Nat. Nanotech.* **12**, 692–700 (2017).
 8. Abbott, N.J., Patabendige, A.A., Dolman, D.E., Yusof, S.R. & Begley, D.J. Structure and function of the blood-brain barrier. *Neurobiol. Dis.* **37**, 13–25 (2010).
 9. St-Amour, I. et al. Brain bioavailability of human intravenous immunoglobulin and its transport through the murine blood-brain barrier. *J. Cereb. Blood Flow. Metab.* **33**, 1983–1992 (2013).
 10. Terstappen, G. C., Meyer, A.H., Bell, R. D. et al. Strategies for delivering therapeutics across the blood-brain barrier. *Nat. Rev. Drug Discov.* **20**, 362–383 (2021).
 11. Agrawal, M. et al. Nose-to-brain drug delivery: an update on clinical challenges and progress towards approval of anti-Alzheimer drugs. *J. Control. Rel.* **281**, 139–177 (2018).
 12. Sabir, F., Ismail, R. & Csoka, I. Nose-to-brain delivery of antiglioblastoma drugs embedded into lipid nanocarrier systems: status quo and outlook. *Drug Discov. Today* **25**, 185–194 (2020).
 13. Bennett, C. F., Krainer, A. R. & Cleveland, D. W. Antisense oligonucleotide therapies for neurodegenerative diseases. *Annu. Rev. Neurosci.* **4**, 385–406 (2019).
 14. Wu, P. Y. et al. Cascade-amplifying synergistic therapy for intracranial glioma via endogenous reactive oxygen species-triggered "all-in-one" nanoplatform. *Adv. Funct. Mater.* 2105786 (2021).
 15. Tang, W. et al. Emerging blood-brain-barrier-crossing nanotechnology for brain cancer theranostics. *Chem. Soc. Rev.* **48**, 2967–3014 (2019).
 16. Cloughesy, T. F., Mochizuki, A. Y., Orpilla, J. R. et al. Neoadjuvant anti-PD-1 immunotherapy promotes a survival benefit with intratumoral and systemic immune responses in recurrent glioblastoma. *Nat. Med.* **25**, 477–486 (2019).
 17. Miura, Y. et al. Cyclic RGD-linked polymeric micelles for targeted delivery of platinum anticancer drugs to glioblastoma through the blood-brain tumor barrier. *ACS Nano* **7**, 8583–8592 (2013).
 18. Pucci, C. et al. Hybrid magnetic nanovectors promote selective glioblastoma cell death through a combined effect of lysosomal membrane permeabilization and chemotherapy. *ACS Appl. Mater. Interfaces* **12**, 29037–29055 (2020).
 19. Yang, Z. et al. Albumin-based nanotheranostic probe with hypoxia alleviating potentiates synchronous multimodal imaging and phototherapy for glioma. *ACS Nano* **14**, 6191–6212 (2020).
 20. Przystal, J. M. et al. Efficacy of systemic temozolomide-activated phage-targeted gene therapy in human glioblastoma. *EMBO Mol. Med.* **11**, e8492 (2019).

21. Park, J. *et al.* Effect of combined anti-PD-1 and temozolomide therapy in glioblastoma. *Oncoimmunology* **8**, e1525243 (2019).
22. Kadiyala, P. *et al.* High-density lipoprotein-mimicking nanodiscs for chemo-immunotherapy against glioblastoma multiforme. *ACS Nano* **13**, 1365–1384 (2019).
23. Guo, J. *et al.* Aptamer-functionalized PEG–PLGA nanoparticles for enhanced anti-glioma drug delivery. *Biomaterials* **32**, 8010–8020 (2011).
24. Wang, C. X. *et al.* Camouflaging nanoparticles with brain metastatic tumor cell membranes: a new strategy to traverse blood-brain barrier for imaging and therapy of brain tumors. *Adv. Funct. Mater.* **30**, 1909369 (2020).
25. Hua, L. *et al.* Hypoxia-responsive lipid-poly- (hypoxic radiosensitized polyprodrug) nanoparticles for glioma chemo-and radiotherapy. *Theranostics* **8**, 5088 (2018).
26. Liu, H. *et al.* Development of a hypoxia-triggered and hypoxic radiosensitized liposome as a doxorubicin carrier to promote synergetic chemo-/radio-therapy for glioma. *Biomaterials* **121**, 130–143 (2017).
27. Aldape, K., Brindle, K. M., Chesler, L. *et al.* Challenges to curing primary brain tumours. *Nat. Rev. Clin. Oncol.* **16**, 509–520 (2019).
28. Tseng, Y. Y. *et al.* Role of polymeric local drug delivery in multimodal treatment of malignant glioma: a review. *Int. J. Nano Med.* **16**, 4597–4614 (2021).
29. Denny, W. A. Hypoxia-activated prodrugs in cancer therapy: progress to the clinic. *Future Oncol.* **6**, 419–428 (2010).
30. Zheng, P. *et al.* Self-propelled and near-infrared-phototoxic photosynthetic bacteria as photothermal agents for hypoxia-targeted cancer therapy. *ACS Nano* **15**, 1100–1110 (2020).
31. Mi, Z. *et al.* “Trojan horse” Salmonella enabling tumor homing of silver nanoparticles *via* neutrophil infiltration for synergistic tumor therapy and enhanced biosafety. *Nano Lett.* **21**, 414–423 (2020).
32. Chen, W. *et al.* Combination of bacterial-photothermal therapy with an anti-PD-1 peptide depot for enhanced immunity against advanced cancer. *Adv. Funct. Mater.* **30**, 1906623 (2020).
33. Yi, X. *et al.* Bacteria-triggered tumor-specific thrombosis to enable potent photothermal immunotherapy of cancer. *Sci. Adv.* **6**, eaba3546 (2020).
34. Kim, K. Mechanisms of microbial traversal of the blood-brain barrier. *Nat. Rev. Microbiol.* **6**, 625–634 (2008).
35. Coureuil, M., Lécuyer, H., Bourdoulous, S. *et al.* A journey into the brain: insight into how bacterial pathogens cross blood–brain barriers. *Nat. Rev. Microbiol.* **15**, 149–159 (2017).
36. Fitzpatrick, Z., Frazer, G., Ferro, A. *et al.* Gut-educated IgA plasma cells defend the meningeal venous sinuses. *Nature* **587**, 472–476 (2020).
37. Sparwasser, T.; Miethke, T.; Lipford, G. *et al.* Bacterial DNA causes septic shock. *Nature* **386**, 336–337 (1997)

38. Chen, W. *et al.* Bacteria-driven hypoxia targeting for combined biotherapy and photothermal therapy. *ACS Nano* **12**, 5995–6005 (2018).
39. Chen, F. *et al.* Nanophotosensitizer-engineered Salmonella bacteria with hypoxia targeting and photothermal-assisted mutual bioaccumulation for solid tumor therapy. *Biomaterials* **214**, 119226 (2019).
40. Kim, K. J., Elliott, S. J., Di Cello, F., Stins, M. F. & Kim, K. S. The K1 capsule modulates trafficking of *E. coli*-containing vacuoles and enhances intracellular bacterial survival in human brain microvascular endothelial cells. *Cell. Microbiol.* **5**, 245–252 (2003).
41. Tang, J., Chu, B., Wang, J. *et al.* Multifunctional nanoagents for ultrasensitive imaging and photoactive killing of Gram-negative and Gram-positive bacteria. *Nat. Commun.* **10**, 4057 (2019).
42. Gowrishankar, G., Namavari, M., Jouannot, E. B. *et al.* Investigation of 6-[¹⁸F]-fluoromaltose as a novel PET tracer for imaging bacterial infection. *PLoS ONE* **9**, e107951 (2014).
43. Namavari, M., Gowrishankar, G., Hoehne, A. *et al.* Synthesis of [¹⁸F]-labelled maltose derivatives as PET tracers for imaging bacterial infection. *Mol. Imaging Biol.* **17**, 168–176 (2015).
44. Gowrishankar, G., Hardy, J., Wardaket, M. *et al.* Specific imaging of bacterial infection using 6-¹⁸F-fluoromaltotriose: a second generation PET tracer targeting the maltodextrin transporter in bacteria. *J. Nucl. Med.* **58**, 1679–1684 (2017).
45. Ning, X., Lee, S., Wang, Z. *et al.* Maltodextrin-based imaging probes detect bacteria *in vivo* with high sensitivity and specificity. *Nat. Mater.* **10**, 602–607 (2011).
46. Takemiya, K., Ning, X., Seo, W. *et al.* Novel PET and near infrared imaging probes for the specific detection of bacterial infections associated with cardiac devices. *JACC-Cardiovasc. Imag.* **12**, 875–886 (2019).
47. Wang, J. *et al.* Designing immunogenic nanotherapeutics for photothermal-triggered immunotherapy involving reprogramming immunosuppression and activating systemic antitumor responses. *Biomaterials* **255**, 120153 (2020).
48. Chen, Q., Xu, L., Liang, C. *et al.* Photothermal therapy with immune-adjuvant nanoparticles together with checkpoint blockade for effective cancer immunotherapy. *Nat. Commun.* **7**, 13193 (2016).
49. Jia, Y.P. *et al.* Multifunctional nanoparticle loaded injectable thermoresponsive hydrogel as NIR controlled release platform for local photothermal immunotherapy to prevent breast cancer postoperative recurrence and metastases. *Adv. Funct. Mater.* **30**, 2001059 (2020).
50. Huang, X. H.; Pan, J. M.; Xu, F. N.; Shao, B. F.; Wang, Y.; Guo, X.; Zhou, S. B. Bacteria-based cancer immunotherapy. *Adv. Sci.* **8**, 2003572 (2021).
51. Fan, J. X. *et al.* Antibody engineered platelets attracted by bacteria-induced tumor-specific blood coagulation for checkpoint inhibitor immunotherapy. *Adv. Funct. Mater.* **31**, 2009744 (2021).
52. Masuko, T. *et al.* Carbohydrate analysis by a phenol–sulfuric acid method in microplate format. *Anal. Biochem.* **339**, 69–72 (2005).

53. Leary, S. C. *et al.* Chronic treatment with azide in situ leads to an irreversible loss of cytochrome c oxidase activity via holoenzyme dissociation. *J. Biol. Chem.* **277**, 11321–11328 (2002).
54. Palucka, K., Banchereau, J. Cancer immunotherapy via dendritic cells. *Nat. Rev. Cancer* **12**, 265–277 (2012).
55. Janeway, C. A.; Bottomly, K. Signals and signs for lymphocyte responses. *Cell* **76**, 275–285 (1994).
56. Li, G. *et al.* Permeability of endothelial and astrocyte cocultures: in vitro blood-brain barrier models for drug delivery studies. *Ann. Biomed. Eng.* **38**, 2499–2511 (2010).
57. Brown, R.C., Morris, A.P. & O'Neil, R.G. Tight junction protein expression and barrier properties of immortalized mouse brain microvessel endothelial cells. *Brain Res.* **1130**, 17–30 (2007).
58. Zhou, S., Gravekamp, C., Bermudes, D. *et al.* Tumour-targeting bacteria engineered to fight cancer. *Nat. Rev. Cancer* **18**, 727–743 (2018).
59. Agrawal, N. *et al.* Bacteriolytic therapy can generate a potent immune response against experimental tumors. *Proc. Natl. Acad. Sci. U.S.A.* **101**, 15172-15177 (2004).
60. Tyrkalska, S. D. *et al.* Neutrophils mediate Salmonella Typhimurium clearance through the GBP4 inflammasome-dependent production of prostaglandins. *Nat. Commun.* **7**, 12077 (2016).
61. Ye, Y. *et al.* A melanin-mediated cancer immunotherapy patch. *Sci. Immunol.* **2** (2017).

Figures

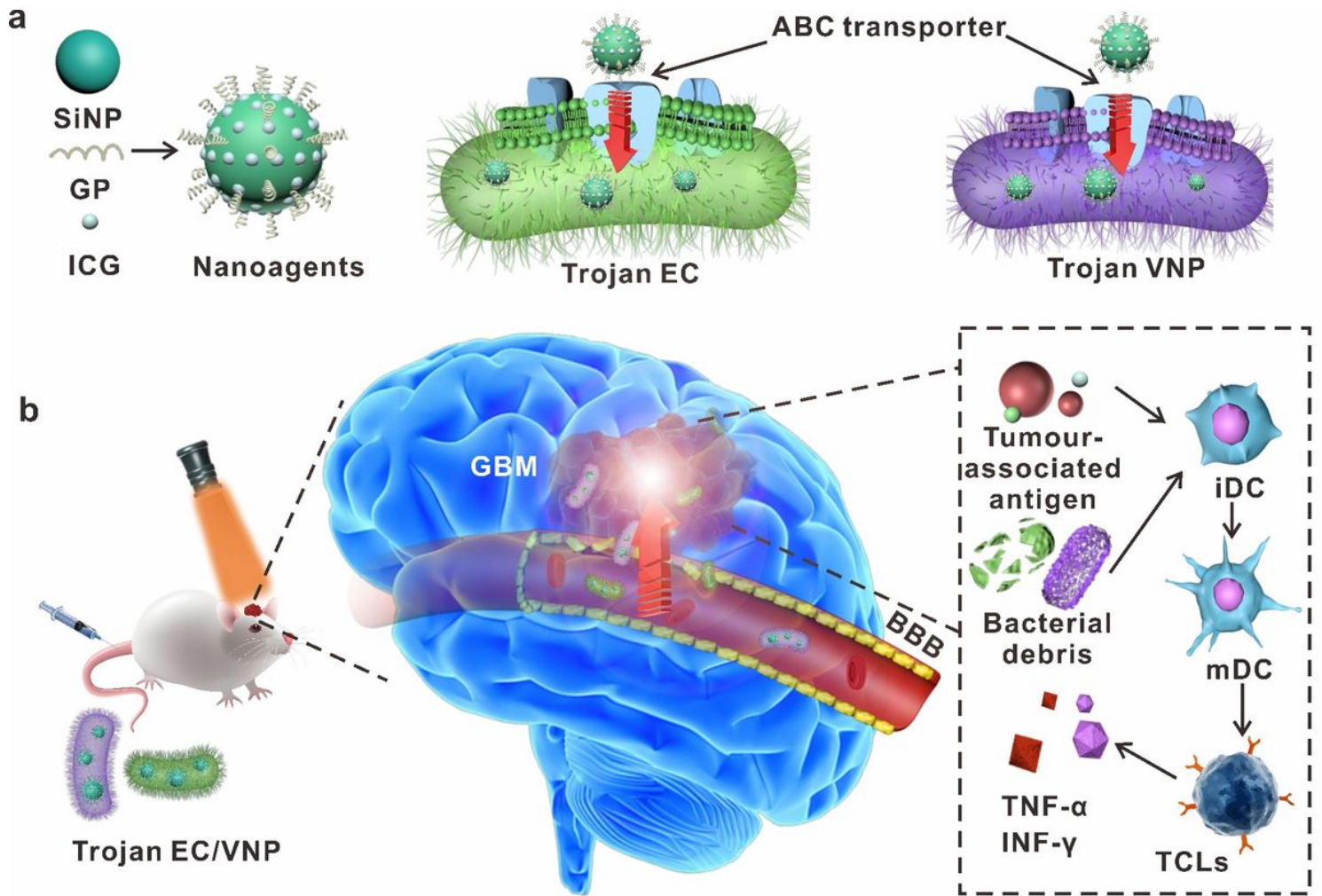


Figure 1

Schematic illustration of Trojan bacteria crossing blood-brain barrier for photothermal immunotherapy of glioblastoma. **a**, A scheme illustrating the construction of Trojan bacteria system. The nanoagents composed of silicon nanoparticle (SiNP) modified with glucose polymer (GP) (e.g., poly[4-O-(α -D-glucopyranosyl)-D-glucopyranose]) and indocyanine green (ICG) were internalized into bacterial cells (e.g., attenuated *Salmonella typhimurium* VNP20009 (VNP), *Escherichia coli* 25922 (EC)) through the bacteria-specific ATP-binding cassette (ABC) transporter to form the Trojan bacteria system (Trojan EC/VNP). **b**, A scheme illustrating Trojan bacteria system crossing the blood-brain barrier (BBB), targeting and penetrating glioblastoma (GBM) tissues, followed by light-triggered photothermal immunotherapy of GBM *in vivo*.

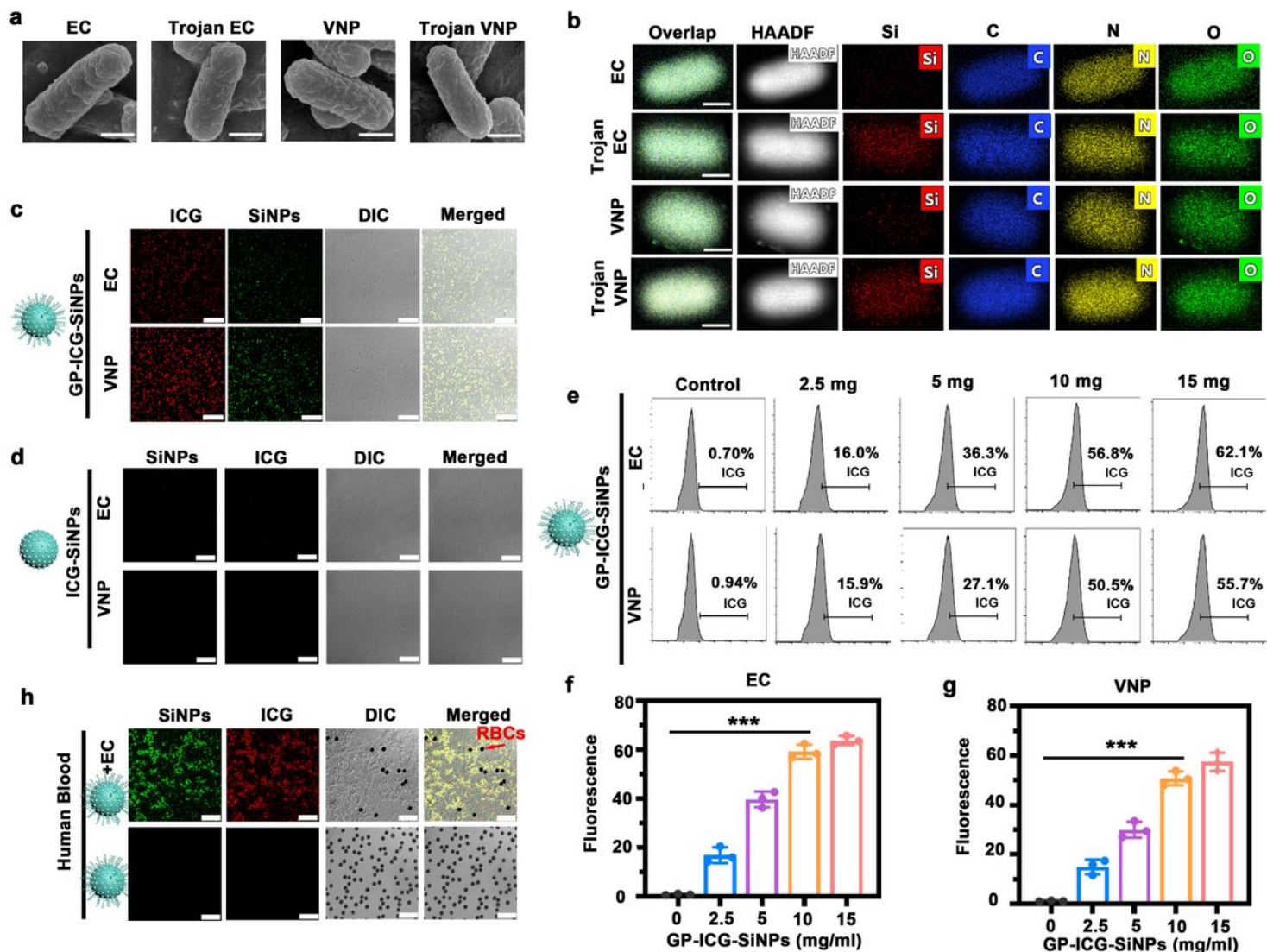


Figure 2

Construction and characterization of Trojan bacteria system. a, SEM images of EC, Trojan EC, VNP and Trojan VNP. Scale bars: 200 nm. b, Elemental mapping in HAADF-STEM images of EC, Trojan EC, VNP and Trojan VNP. Scale bars: 500 nm. c, CLSM images of EC and VNP incubated with GP-ICG-SiNPs. Scale bars: 25 μ m. d, CLSM images of EC and VNP incubated with ICG-SiNPs. Scale bars: 25 μ m. e-g, Flow cytometry analysis of the uptake rates of EC and VNP incubated with different concentrations of GP-ICG-SiNPs for 2 h (e) and corresponding quantitative analysis of uptake rates of different concentrations of GP-ICG-SiNPs by EC (f) and VNP (g). h, CLSM images of the mixture of human blood and EC after incubation with GP-ICG-SiNPs. Arrows indicate red blood cells (RBCs). Scale bars: 25 μ m. The EC or VNP were incubated with the synthesized nanoagents ([SiNPs] = 12 mg/mL, [ICG] = 600 μ g/mL) at 37 oC for 2 h. After incubation, the treated bacteria were rinsed with PBS buffer for several times. The bacterial cell concentration is $\sim 1.0 \times 10^7$ CFU. All error bars represent the standard deviation determined from three independent assays. All data are presented as means \pm SD. Statistical significance is calculated via one-way analysis of variance (ANOVA) with a Tukey post-hoc test (***)P < 0.001).

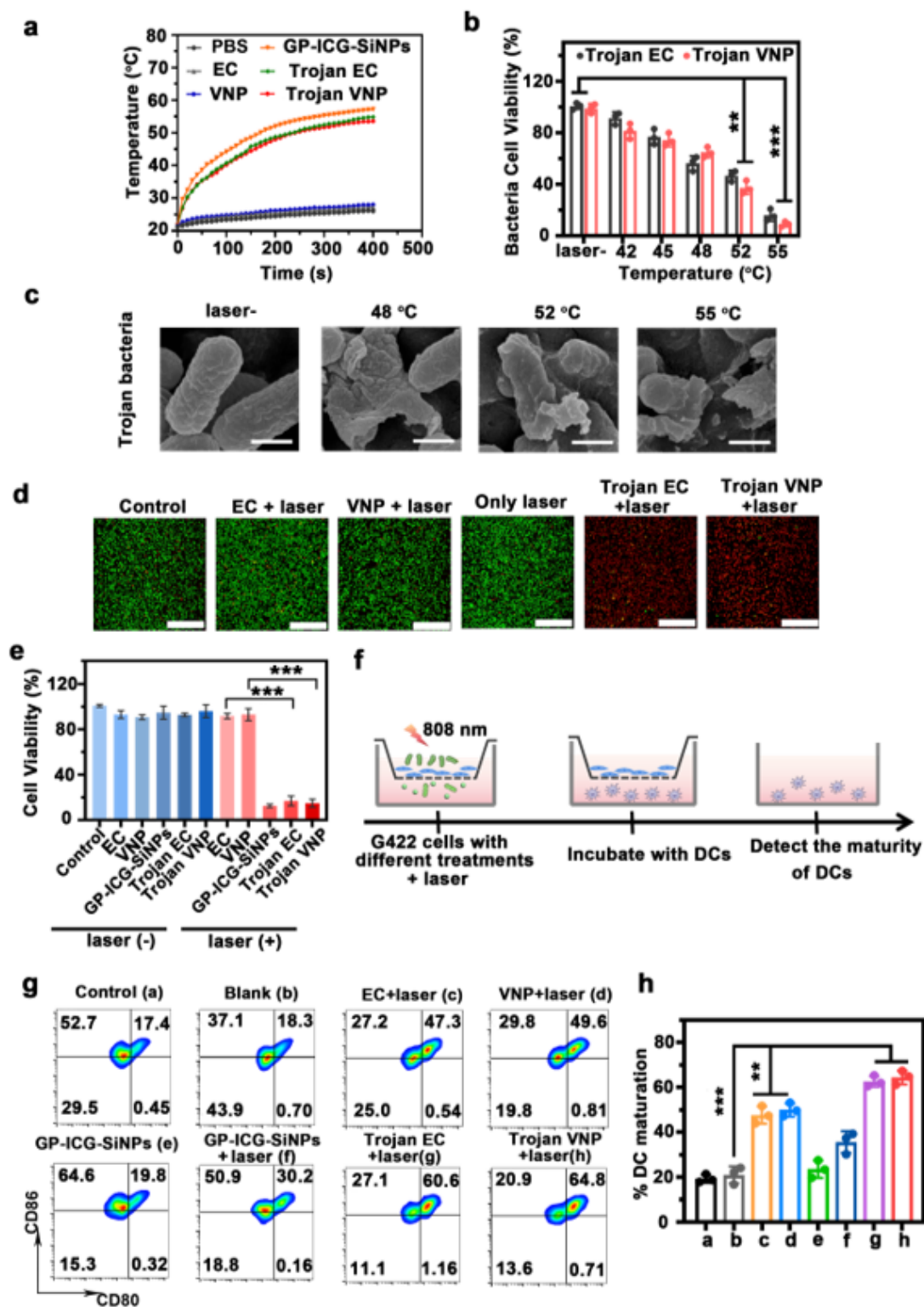


Figure 3

Trojan bacteria system against tumour in vitro. a, Photothermal heating curves of PBS, GP-ICG-SiNPs, EC, VNP, Trojan EC and Trojan VNP under the irradiation of NIR laser (808 nm, 1.2 W/cm²). b, The viability of Trojan EC or Trojan at different temperatures (mean \pm SD, n = 3, **P < 0.01, ***P < 0.001). c, SEM images of Trojan bacteria at different temperatures. Scale bars: 200 nm. d, Confocal fluorescence images of G422 cells stained with calcein AM (CAM) and PI after treated with PBS, EC, VNP, GP-ICG-SiNPs, Trojan EC

and Trojan VNP with or without laser irradiation for 5 minutes (808 nm, 1.2 W/cm²). Scale bars: 500 μm. e, The viability of G422 cells treated with EC, VNP, GP-ICG-SiNPs, Trojan EC and Trojan VNP with or without laser irradiation for 5 minutes (808 nm, 1.2 W/cm²) (mean ± SD, n = 3, ***P < 0.001). f, Schematic diagram of the transwell system. G422 cells were cultured in the upper chamber and DCs were cultured in the lower chamber. g, Flow cytometry analysis of CD86 and CD80 expression of G422 cells treated with PBS, EC, VNP, GP-ICG-SiNPs, Trojan EC and Trojan VNP with laser irradiation for 5 minutes (808 nm, 1.2 W/cm²). h, Quantification of the maturation of DCs after treatment for 20 h in the transwell system (mean ± SD, n = 3, **P < 0.01). The bacterial cell concentration is ~10⁷ CFU. Statistical significance was calculated via one-way analysis of variance (ANOVA) with a Tukey post-hoc test.

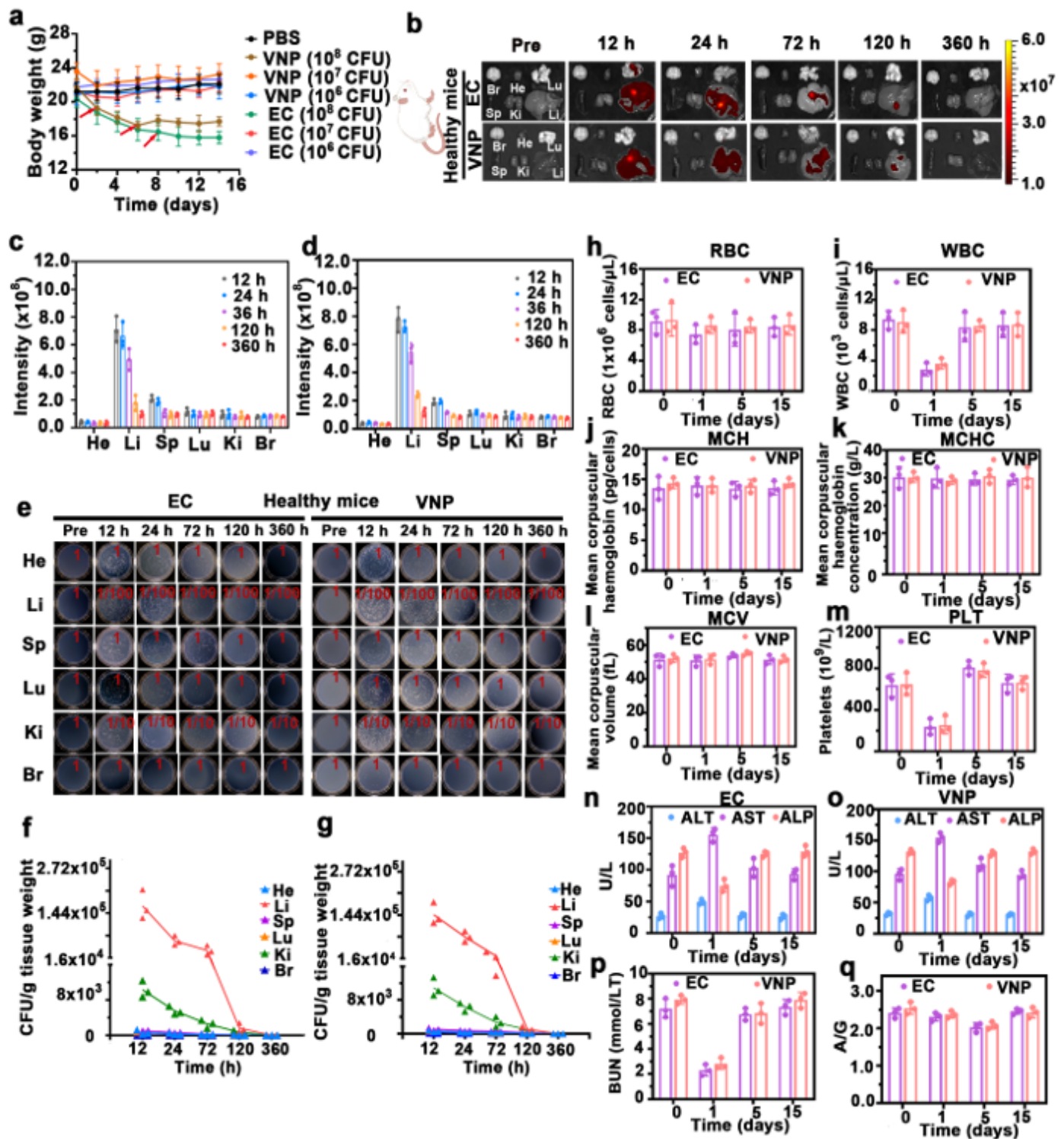


Figure 4

In vivo behaviors of bacteria in mice. a, Average body weights of healthy mice injected with EC or VNP with different concentrations. The red arrow indicates the death of mice. Data are presented as the mean \pm SEM. b-d, Ex vivo fluorescence images of major organs (heart, liver, spleen, lung, kidney and brain) of healthy mice after the intravenous injection with mCherry@EC and mCherry@VNP at the dose of $\sim 1 \times 10^7$ CFU for 12, 24, 72, 120 and 360 h (b) and corresponding fluorescence intensity in mCherry@EC group (c)

and mCherry@VNP group (d). Data are presented as the mean \pm SEM. e-g, Homogenates of major organs of healthy mice after intravenous injection with mCherry@EC (left) and mCherry@VNP (right) for 12, 24, 72 120 and 360 h cultured on the solid LB agar (n=3) (e) and corresponding quantification of bacterial colonization in mCherry@EC group (f) and mCherry@VNP group (g). h-q, Blood biochemistry and hematology data of healthy female Balb/c mice intravenously injected with EC or VNP at the dose of 1.0×10^7 CFU per mouse at 1, 5, and 15 d post injection. Time-course changes of red blood cells (h), white blood cells (i), mean corpuscular hemoglobin (j), mean corpuscular hemoglobin concentration (k), mean corpuscular volume (l), and platelets (m). Glutamic-pyruvic transaminase (ALT), alkaline phosphatase (ALP), and aspartate aminotransferase (AST) levels in the blood at various time points after injection with EC (n) and VNP (o). (p) Blood urea nitrogen (BUN) over time. (q) Time-course albumin/globin ratios.

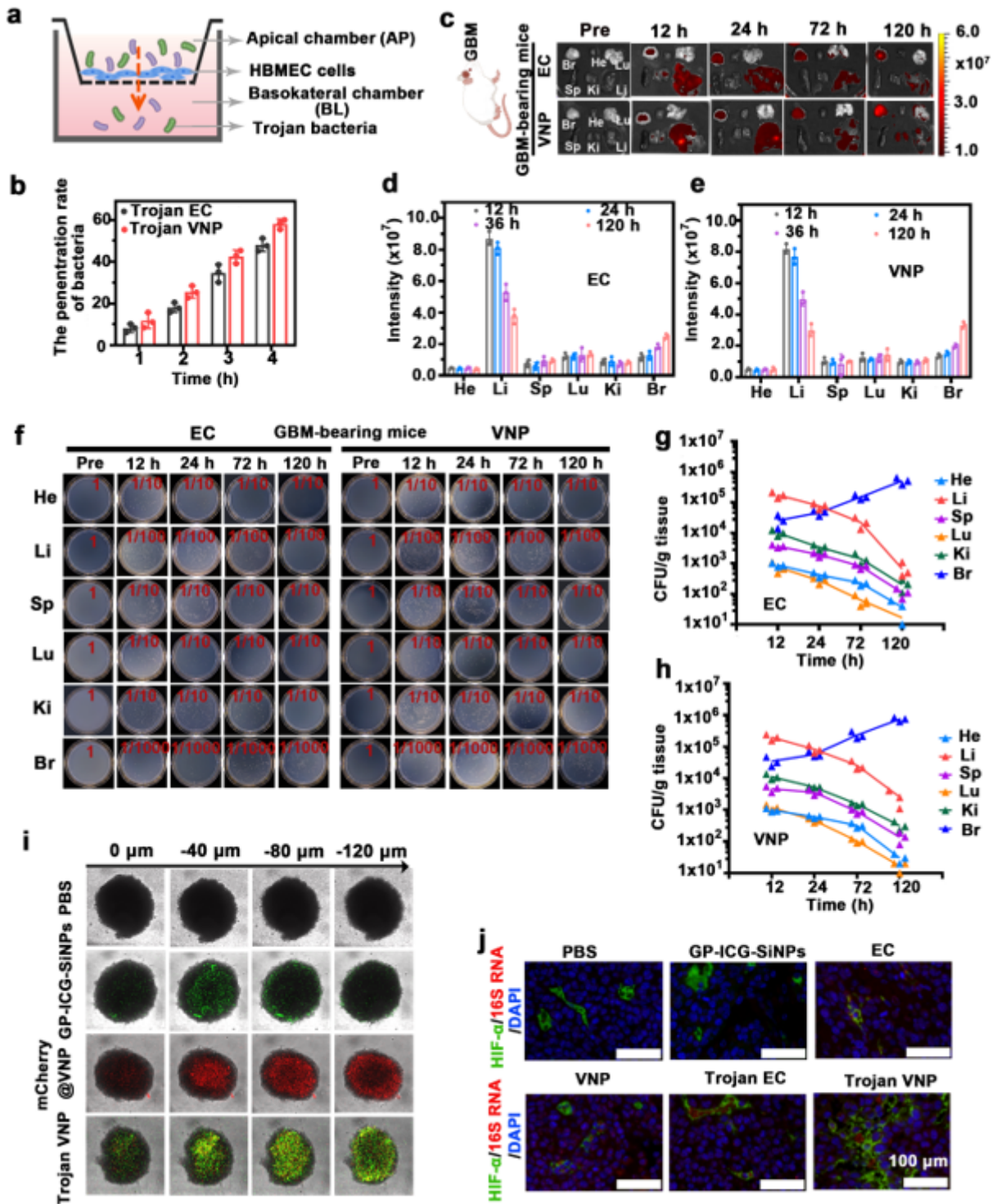


Figure 5

Trojan bacteria crossing BBB, targeting and penetrating GBM. a, Schematic diagram of in vitro BBB model for evaluating whether the Trojan bacteria could cross the BBB. b, The corresponding penetration rates of Trojan EC or Trojan VNP at 1, 2, 3 and 4h (mean \pm SD, n = 3). c-e, Ex vivo fluorescence images of major organs (heart, liver, spleen, lung, kidney and brain) of GBM-bearing mice after intravenous injection with mCherry@EC and mCherry@VNP at the dose of $\sim 1 \times 10^7$ CFU for 12, 24, 72 and 120 h (c) and corresponding fluorescence intensity in mCherry@EC group (d) and mCherry@VNP group (e) (mean \pm SD,

n = 3). f-h, Homogenates of major organs of GBM-bearing mice after intravenous injection with mCherry@EC (left) and mCherry@VNP (right) for 12, 24, 72 and 120 h cultured on the solid LB agar (n=3) (f) and corresponding quantification of bacterial colonization in mCherry@EC group (g) and mCherry@VNP group (h) (mean \pm SD, n = 3). i, Penetration of Trojan bacteria in 3D tumor microspheres. j, In situ hybridization fluorescence image of GBM tissues. The nucleus, hypoxic zone and bacteria were stained with DAPI (blue), anti-HIF- α antibody (green) and 16S RNA probe (red), respectively. Scale bars: 100 μ m.

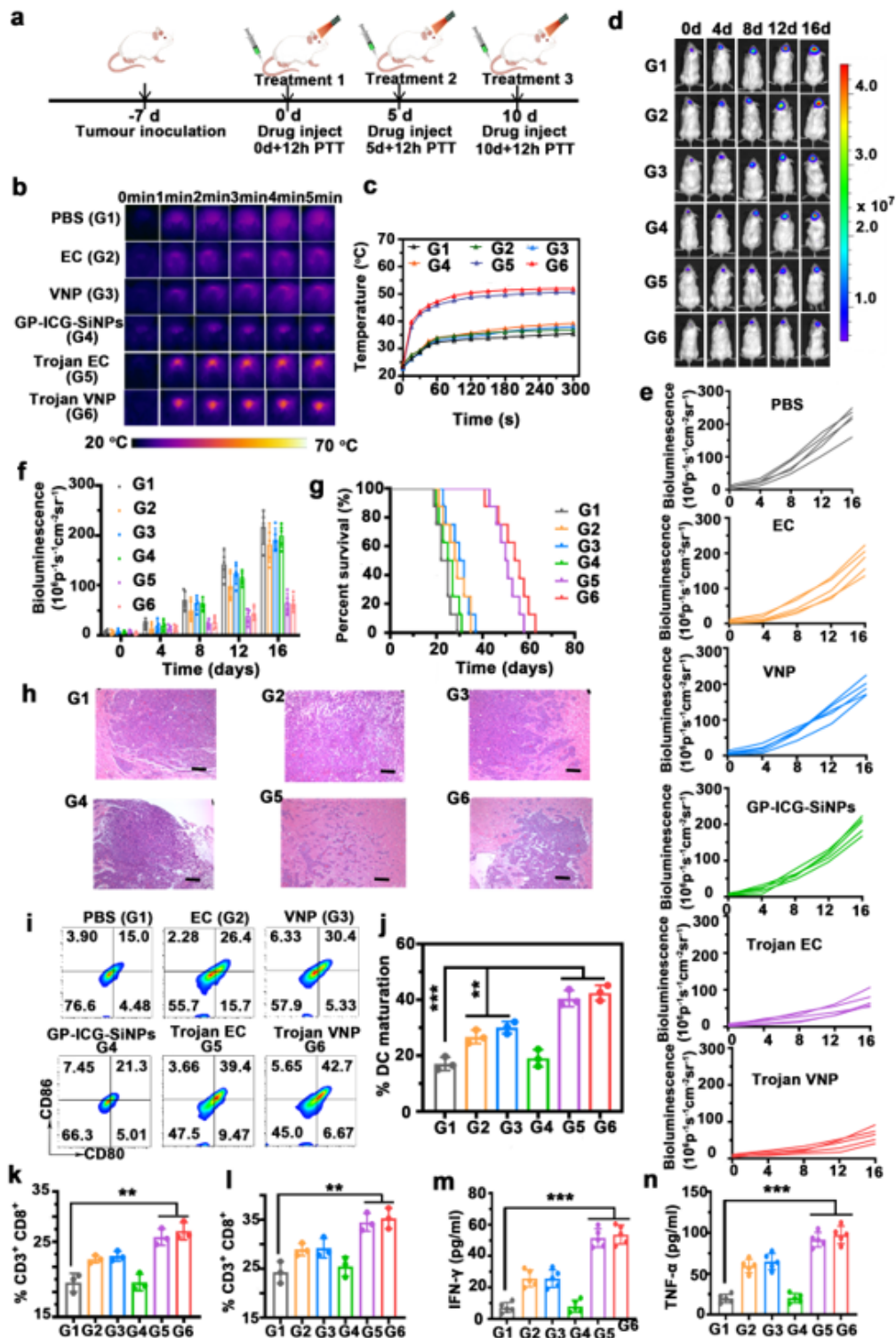


Figure 6

Trojan bacteria-induced photothermal immunotherapy. a, Schematic illustrating Trojan bacteria therapy in a GBM-bearing mouse model. b-c, Representative infrared images of the brains of GBM-bearing mice treated with PBS (G1), EC (G2), VNP (G3), GP-ICG-SiNPs (G4), Trojan EC (G5) and Trojan VNP (G6) under 808 nm laser irradiation (b) and the corresponding temperature changes of brains in different treatment groups (c). d-f, Representative in vivo bioluminescence images of GBM-bearing mice (d), individual bioluminescence change curves (e) and the semi-quantification of bioluminescence intensity of brains in different groups during treatment (f) (mean \pm SD, n = 5). g, Kaplan-Meier survival curves. h, The H&E staining analysis on the brain tissue of GBM-bearing mice in different groups after therapy. Scale bars: 250 μ m. i, Representative flow cytometry plots of DC maturation in draining lymph nodes of GBM tumour-bearing mice after therapy. After 3 days of different treatments, DCs were obtained from the lymph nodes of the carotid artery drainage of mice. The obtained DCs were stained with CD11c, CD80, CD86 and analyzed by flow cytometry. j, Quantification of DC maturation (mean \pm SD, n = 3, **P < 0.01, ***P < 0.001). k, Qualification of CD3⁺ CD8a⁺ T cells in splenocytes by flow cytometry (mean \pm SD, n = 3, **P < 0.01). l, Qualification of CD3⁺ CD8a⁺ T cells in tumour by flow cytometry (mean \pm SD, n = 3, **P < 0.01). m, Qualification of IFN- γ in serum of GBM tumour-bearing mice on the 16th day after treatment (mean \pm SD, n = 3, ***P < 0.001). n, Qualification of IFN- γ in serum of GBM tumour-bearing mice on the 16th day after treatment (mean \pm SD, n = 3, ***P < 0.001). Statistical significance was calculated via one-way analysis of variance (ANOVA) with a Tukey post-hoc test.

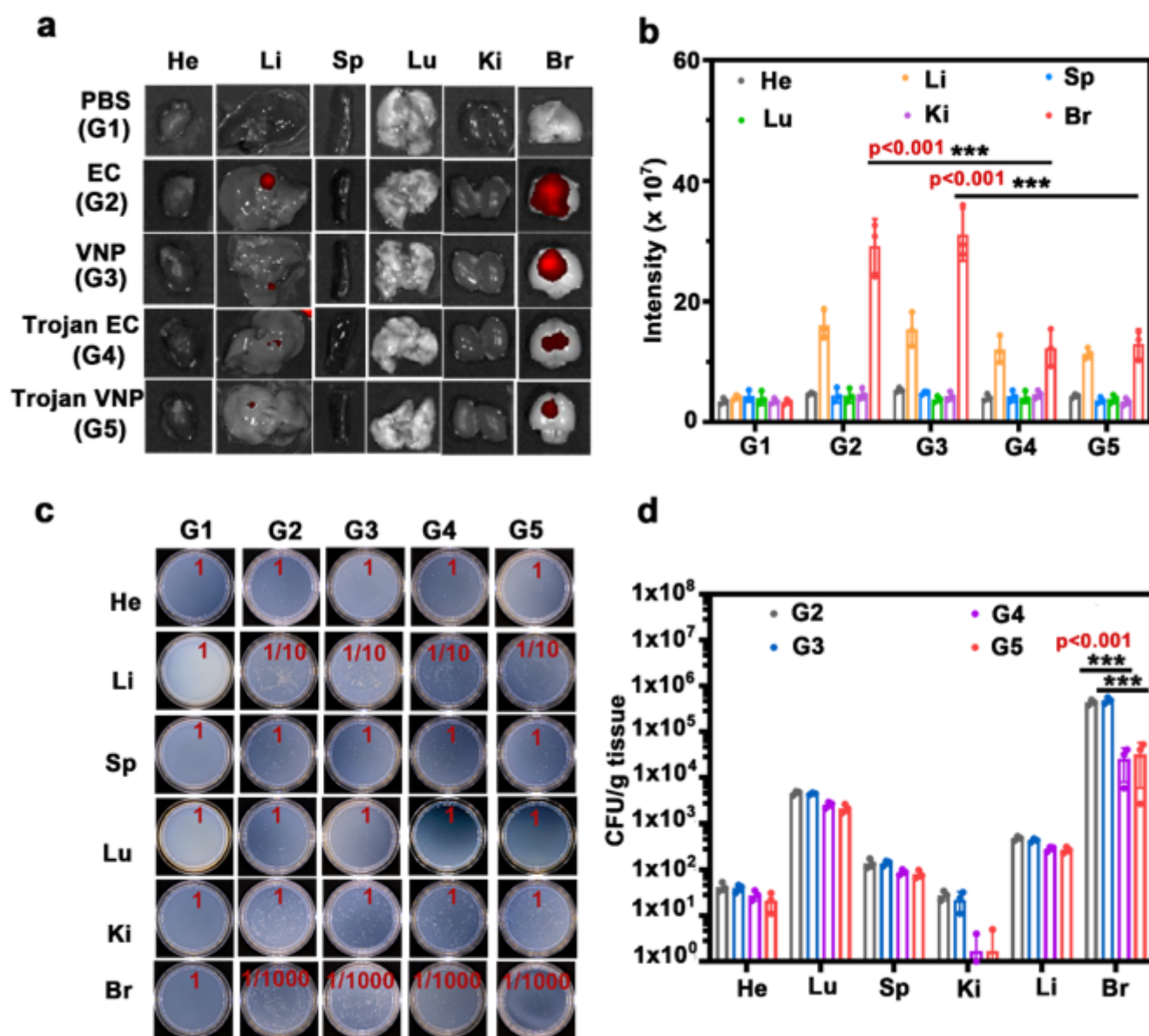


Figure 7

The elimination of residual bacteria after photothermal immunotherapy. a, The fluorescence distribution in the main organs (heart, liver, spleen, lung, kidney and brain) of GBM-bearing mice after photothermal immunotherapy. The mice were intravenously injected with (G1) PBS, (G2) $\sim 1 \times 10^7$ CFU mCherry@EC (m@EC), (G3) $\sim 1 \times 10^7$ CFU mCherry@VNP (m@VNP), (G4) Trojan m@EC (e.g., GP-ICG-SiNPs (8 mg/kg ICG) internalized into $\sim 1 \times 10^7$ CFU m@EC) or (G5) Trojan m@VNP (e.g., GP-ICG-SiNPs (8 mg/kg ICG) internalized into 1×10^7 CFU m@VNP), respectively. At the 12-hour post-injection, the brains of those mice were suffered by an 808 nm irradiation (1.2W/cm², 5 min), followed by ex vivo imaging of the main organs at 5-day. b, The corresponding quantitative analysis of fluorescence intensity of main organs in different groups after photothermal immunotherapy (mean \pm SD, n = 3, ***P < 0.001). c, Homogenates of

major organs of GBM-bearing mice in different groups after photothermal immunotherapy cultured on the solid LB agar. d, Corresponding quantification of bacterial colonization on LB solid plates in different treatment groups (mean \pm SD, n = 3, ***P < 0.001). Statistical significance was calculated via one-way analysis of variance (ANOVA) with a Tukey post-hoc test.

Supplementary Files

This is a list of supplementary files associated with this preprint. Click to download.

- [Checklist.pdf](#)
- [129070sourcedata97958r34518.pdf](#)
- [NCTrojanbacteriacrossBBBforPTTimmunotherapyofGBMSPHefinalversion.docx](#)
- [NCOMMS2147161TRS.pdf](#)